

Probing outbursts of the transient neutron star low mass X-ray binary Aql X-1 with *NICER*: a study of spectral evolution

Karthik Gananath Putha¹*, Yash Bhargava² and Sudip Bhattacharyya²

¹*Department of Physics and Astronomy, University of South Carolina, 712 Main St., Columbia 29205, USA*

²*Department of Astronomy and Astrophysics, Tata Institute of Fundamental Research, 1 Homi Bhabha Road, Colaba, Mumbai 400005, India*

Accepted XXX. Received YYY; in original form ZZZ

ABSTRACT

X-ray observations of neutron star (NS) low mass X-ray binaries (LMXBs) are useful to probe physical processes close to the NS and to constrain source parameters. Aql X-1 is a transient NS LMXB which frequently undergoes outbursts provides an excellent opportunity to study source properties and accretion mechanism in strong gravity regime over a wide range of accretion rates. In this work, we systematically investigate the spectral evolution of Aql X-1 using *NICER* observations during the source outbursts in 2019 and 2020. The *NICER* observations cover the complete transition of the source from its canonical hard state to soft state and back. The spectra extracted from most observations can be explained by a partially Comptonised accretion disc. We find that the system can be described by an accretion disk with an inner temperature of ≈ 0.7 keV and a Comptonising medium of thermal electrons at ≈ 2 keV, while the photon index is strongly degenerate with the covering fraction of the medium. We also find evidence of Fe $K\alpha$ fluorescence emission in the spectra indicating reprocessing of the Comptonised photons. We observe an absorption column density higher than the Galactic column density for most of the observations indicating a significant local absorption. But for some of the observations in 2020 outburst, the local absorption is negligible.

Key words: accretion, accretion discs—methods: data analysis—stars: neutron —X-rays: binaries—X-rays: individual (Aql X-1).

1 INTRODUCTION

Low mass X-ray binaries (LMXB) consists of a neutron star (NS) or a black hole (BH) and a companion star with a mass $\lesssim 1 M_{\odot}$. In these binaries, the compact object accretes the matter from the companion star through the Roche-Lobe overflow. The NS LMXBs are broadly categorised into ‘atoll’ sources or ‘Z’ sources based on the shape of the track generated on their hardness intensity diagram (HID) or the colour-colour diagram (CCD) (see van der Klis 2004, for a review). Most of the NS LMXBs are transient systems which stay in the quiescent phase for long duration and undergo outbursts during which they are typically detected. These systems produce outbursts, due to the increased mass accretion rate, which are caused by the instabilities in the disc (Shakura & Sunyaev 1973; Done et al. 2007). During these outbursts, the luminosity of the system increases and it emits photons from the radio to the X-ray band (Done et al. 2007).

The X-ray emission from NS LMXBs has been modelled with a combination of spectral components. The primary component of the modelling is the accretion disc (Shakura & Sunyaev 1973), a blackbody component (from the accretion mound on the surface of the NS or from the boundary layer) and a non-thermal emission (either from the accretion column or the Comptonised emission). The Comptonised emission results from Compton up-scattering of the soft thermal photons from the accretion disc by a hot plasma of

electrons (often called corona) close to the NS. During the evolution of the source across various accretion states, there is a strong interplay between these components which decides the track followed by the source on the HID/CCD.

Aquila X-1 (or Aql X-1, discovered by Kunte et al. 1973) is one of the most famous NS LMXBs which regularly goes into an outburst every year (although the outburst is not exactly periodic, Šimon 2002; Ootes et al. 2018). Due to the extensive observations of the source in various wavelengths, key parameters of the source are well known. Aql X-1 has a K-type donor and is placed at a distance of 6 ± 2 kpc (Mata Sánchez et al. 2017). The orbital period of the binary system is 18.95 d (Chevalier & Ilovaisky 1991; Welsh et al. 2000). The presence of the thermo-nuclear bursts in the X-ray light curves suggest the compact object is a NS (e.g. Galloway et al. 2008; Güver et al. 2022) and the detection of the millisecond pulsations in one such bursts (1.8 ms, Casella et al. 2008) confirms the nature of the accretor. Aql X-1 is one of the few NS LMXBs which shows a hysteresis in the HID (Maitra & Bailyn 2004; Güver et al. 2022) similar to BH LMXBs (e.g. Bhargava et al. 2019; Rawat et al. 2023, and references within). Using *RXTE*-PCA observations of Aql X-1, Maitra & Bailyn (2004) have studied the evolution of the source across the outburst in 2000 as it traverses various spectral states i.e. low hard state (LHS) and high soft state (HSS) and other intermediate states. The authors characterise the spectrum of the source as a combination of an accretion disc and a powerlaw component. Similar characterisation of the source evolution across different types of the outbursts (i.e. long high, medium low and short low) was conducted using monitoring

* E-mail: kputha@email.sc.edu

observations of Aql X-1 with *RXTE/PCA* by [Güngör et al. \(2014\)](#). The long high outbursts are more frequent and during the majority of the outburst, the source stays in the HSS while tracing a hysteresis across the other states during the rise and the decay phase of the outburst ([Maitra & Bailyn 2004](#)). [López-Navas et al. \(2020\)](#) have undertaken preliminary investigation of the soft X-ray evolution of the source using *Swift-XRT* spectra but mainly focus on the correlation of the UV-optical properties and their correlation with the X-ray spectral evolution. Recently, [Niwanu et al. \(2023\)](#) studied outbursts of the source from 2016–2019 using the *MAXI* instrument onboard ISS where they model the 2–20 keV spectrum as the emission from an absorbed accretion disc.

The soft X-ray evolution of NS LMXB holds the key to evolution of the thermal components (e.g. [Bhargava et al. 2023](#)). In case of Aql X-1, the soft X-ray spectrum is somewhat understudied. In this article, we investigate the properties of Aql X-1 in soft X-rays using extensive *NICER* monitoring during its outbursts in 2019 and 2020. We report the details of the observation and data reduction methods in section 2, spectral analysis methodology in section 3 and describe the results and our interpretation in section 4.

2 OBSERVATIONS AND DATA REDUCTION

NICER ([Gendreau et al. 2016](#)) has regularly observed Aql X-1 since its launch in 2017. Since then Aql X-1 has undergone several outbursts. For this analysis, we consider the outbursts that happened from 2019 August 2 - 2019 September 21 (outburst A) and from 2020 August 15 - 2020 October 23 (outburst B). These observations are considered for the analysis as they are representative of the complete outburst (from the rise to the decay). The details of the observations are reported in tables A1 and A2. In the draft, we refer to the observations with A/BXXX, where A/B denote which outburst they are part of and the XXX indicates the last three digits of the observation id (ObsID) as mentioned in tables A1 and A2.

The data is processed through a standard filtering pipeline, using `nicer12` i.e. excluding the detectors 14, 34 and excluding the time intervals corresponding to South Atlantic Anomaly (SAA) passages, the Earth elevation angle $> 15^\circ$, the elevation angle with respect to the bright Earth limb $\leq 30^\circ$, and considering the intervals where the undershoot and overshoot count rates per module are 0–500 and 0–30 respectively. We used HEASOFT V6.31, NICERDAS V10a and CALDB version xti20221001.

Using `nicer13-1c`, light curves are extracted in the energy ranges 0.5–12.0 keV, 0.5–2.0 keV, and 2.0–5.0 keV. For further analysis, we ignore the observations with the net exposure ≤ 200 s. We depict the light curves in 0.5–12 keV in the top panels of figure 1 and the hardness ratio of computed using 2–5 keV and 0.5–2 keV light curves in the bottom panels of figure 1. We also construct a HID of the source for both the outbursts in figure 2. Some of the observations analysed here show bursts in their light curve. Since we want to focus on the persistent emission of the source, we identify the time stamps of the bursts from the light curve using `xselect` and create Good Time Intervals (GTIs) excluding the bursts¹. Information about these bursts are listed in table A3. To exclude the burst, we remove the interval during which the source exceeded the mean count rate before and after the burst, without assuming any decay timescale. These GTIs are then passed to `nicer13-spec` routine while extracting the spectrum.

¹ <https://swift.gsfc.nasa.gov/analysis/threads/batlightcurvethread.html>, is used to construct GTI

The burst intervals have been excluded from the light curves plotted in the above-mentioned figures and the further spectral analysis.

3 SPECTRAL ANALYSIS

To investigate the spectral evolution of Aql X-1, we characterise the spectrum as seen by *NICER* in 0.5–10 keV for all the observations. For modelling the spectrum, we use the χ^2 -statistic and report the 1σ uncertainty in the parameters throughout the article. We use the SCORPEON model ([Markwardt et al. 2023](#)) to estimate the background, and fix the background model parameters to the default values. In case of the fainter observations (count rate in 0.5–12 keV ≤ 100 cts/s, B149–B159), we restrict the spectrum to the energy ranges where the source counts are above the expected background level. A systematic error of 0.8% is used during the spectrum modelling in the operational energy range of 0.5–10 keV. We have used the optimal binning by the spectral response ([Kaastra & Bleeker 2016](#)) for the spectral modelling. We have depicted spectrum of observation A116 in the top panel of the figure 3.

To test the nature of the spectrum, we model the spectra from the individual observations with, a single additive component (viz. `diskbb`, `bbodyrad` or `nthcomp`), along with an absorption model to correct for the interstellar+intrinsic absorption (modelled with `tbabs`). The abundances from [Wilms et al. \(2000\)](#) and the cross-sections from [Verner et al. \(1996\)](#) are used to model the spectrum. The single-component model is found to be insufficient to explain the spectrum with count rate > 100 counts. For example, ObsID A121 the model `tbabs*(diskbb)` result in $\chi^2/\text{degrees of freedom (DoF)}$ of 8852.37/158, but on inclusion of Comptonisation model `thcomp` ([Zdziarski et al. 2020](#)) result in χ^2/DoF of 144.22/156. The drastic change in χ^2 for a minimal change in the DoF indicates a strong presences of a Comptonized emission. Thus we model all the spectra at least as a combination of a thermalised accretion disc and a Comptonised emission i.e. `tbabs*(thcomp@diskbb)`. Across all ObsIDs (except the fainter observations, i.e. B151–B159), we identify residuals around 0.75 keV which can be modelled by a Gaussian. This feature has also been seen in other sources with *NICER* indicating that it is an instrumental feature (e.g. [Zhang et al. 2023](#)). For example, in A112, adding a Gaussian component reduces χ^2/DoF from 191.97/143 to 153/140, resulting in a f-test statistic of 11.88 and probability of 5.55×10^{-7} . Thus we model the observations by including the Gaussian in the model (`tbabs*(gauss+thcomp@diskbb)`; Model A). The residuals of some spectra indicate the presence of a weak Fe $K\alpha$ emission line which is modelled by a Gaussian, i.e. `Tbabs*(gauss+gauss+thcomp@diskbb)` (Model B). For example, the addition of Gaussian for A116 (which shows a structured residual near 6.5 keV with Model A) results in a f-test value of 22.55 with probability 2.97×10^{-9} , whereas adding a Gaussian to A112 (with no significant residual near 6.5 keV with Model A) results in an f-test value of 2.84 with probability 0.061. Some observations at the end of outburst B, i.e. from B151–B153 do not show evidence for the instrumental Gaussian component and are modelled by `tbabs*(thcomp@diskbb)`; (Model C) and fainter observations B154–B159 are modelled by `tbabs*(diskbb)` (Model D). We depict the spectrum and its spectral decomposition of A116 in the first panel of figure 3 and the residuals to the spectral fits in the bottom panels of figure 3. The second panel shows the residuals with both Gaussians, third panel shows the residual without the Gaussian at 6.5 keV and last panel displays the residual with out Gaussian at 0.75 keV.

The convolution model `thcomp` up-scatters a fraction of the seed

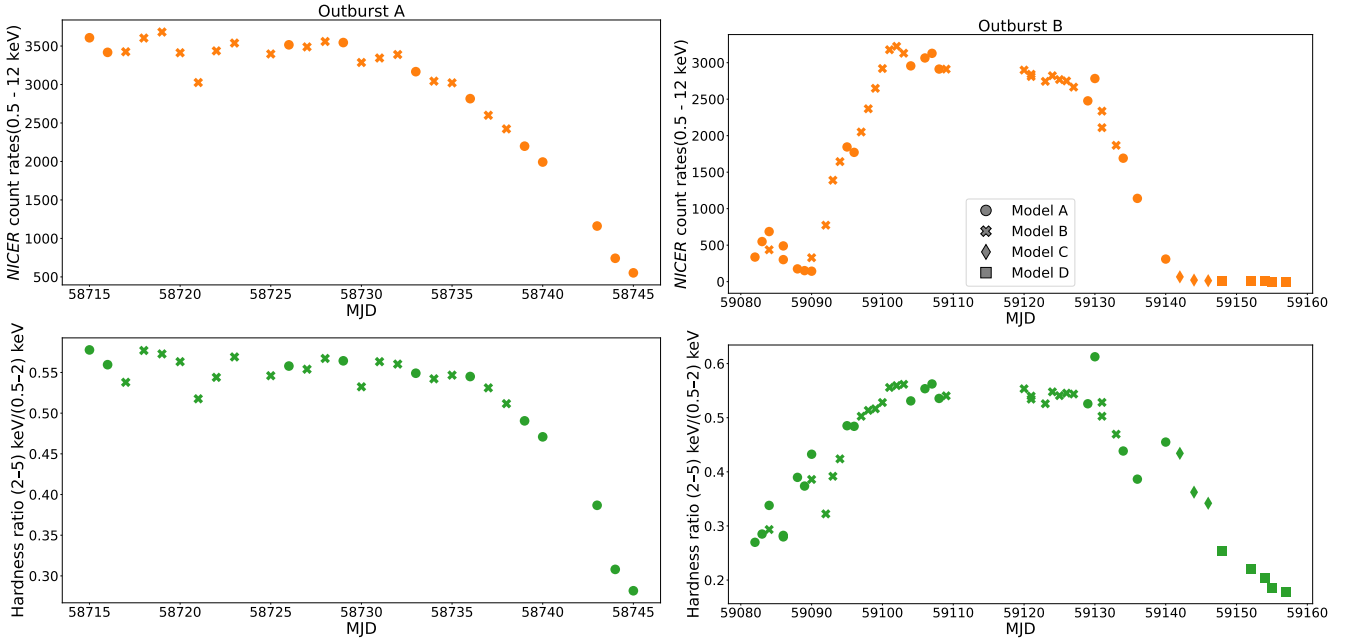


Figure 1: The plots have been updated Outburst of Aql X-1 in 2019 (left panels) and 2020 (right panels). The top panels (both left and right) show the evolution of the count rate in 0.5–12 keV while the bottom panels show the evolution of the hardness ratio in 2–5/0.5–2 keV energy bands. Each point corresponds to a single observation. The shape of the points have been assigned according to the spectral decomposition, i.e., Model A = $\text{tbabs} * (\text{gauss} + \text{thcomp} \otimes \text{diskbb})$ by a circle, Model B = $\text{tbabs} * (\text{gauss} + \text{gauss} + \text{thcomp} \otimes \text{diskbb})$ by a cross, Model C = $\text{tbabs} * (\text{thcomp} \otimes \text{diskbb})$ by a diamond, and Model D = $\text{tbabs} * (\text{diskbb})$ by a square (see the text for a detailed description of the models).

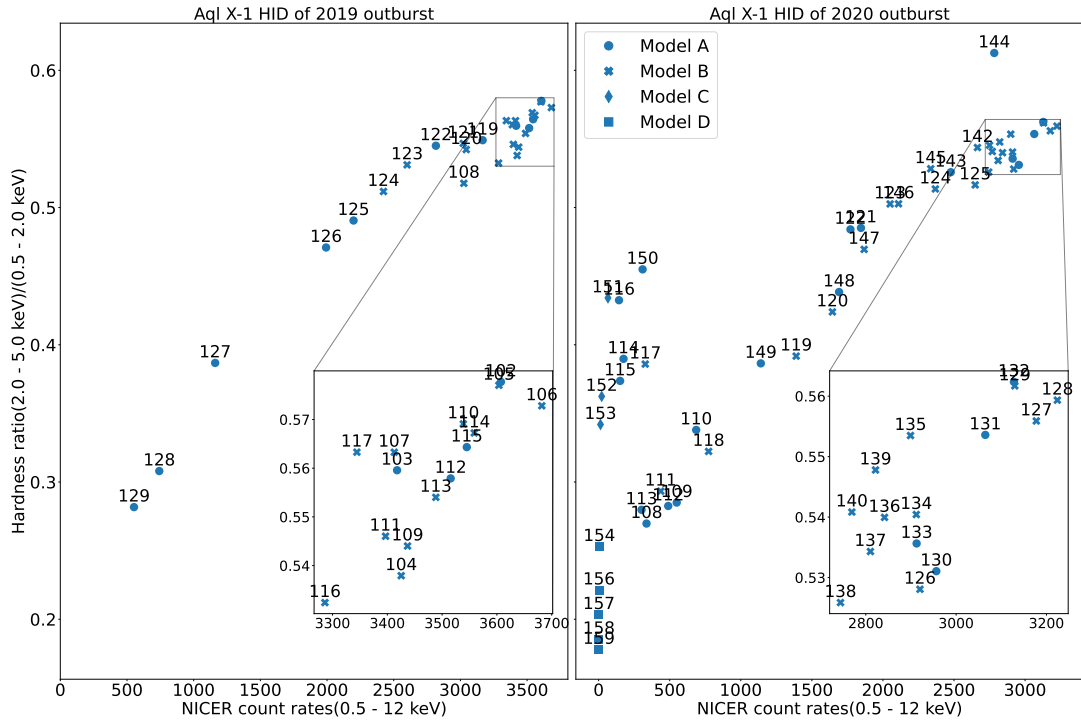


Figure 2: The plot has been updated Hardness intensity diagram of 2019 (left panel) and 2020 (right panel) outbursts of Aql X-1. Hardness ratio is defined as the ratio between the 2–5 and 0.5–2 keV light curve is plotted against the intensity in 0.5–12 keV energy range. The inset plot shows a better view of the clustered points in the HSS. The marker scheme is same as Figure 1.

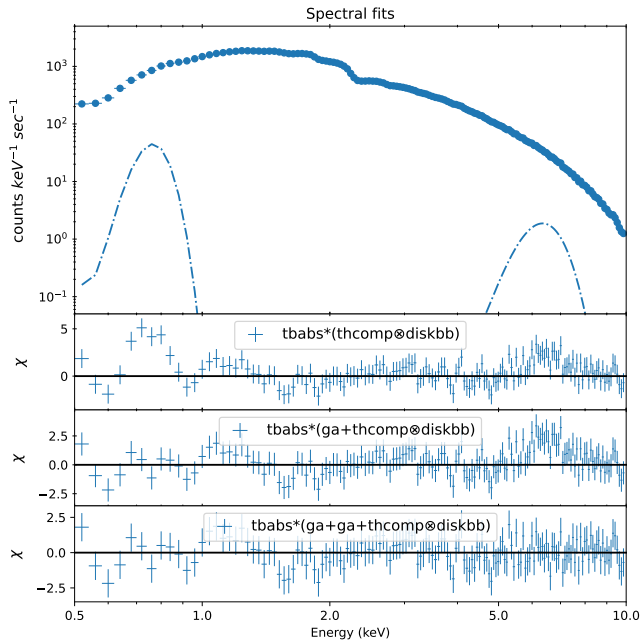


Figure 3: Count spectra and spectral decomposition (top panel), and residuals ($\chi = (\text{Data} - \text{Model})/\text{Error}$) without both Gaussians (second panel), without Gaussian for iron line (third panel) and with both Gaussians (bottom panel) for A116 observation with the model B having a fixed covering fraction $f=0.75$.

photons (f) from the disc and returns a combination of the unscattered disc emission and Comptonised emission (of a photon index Γ and electron temperature kT_e). Since convolution models requires computation of the model beyond the spectral fitting range, we used a custom energy grid from 0.01–100 keV using 1000 logarithmic bins.

If we keep all parameters free across the different observations, we find that some of the observations indicated a low Γ (~ 1) while some required high Γ (~ 1.8), while they lie at a similar HID position. These observations also show low and high f respectively. To probe if there is a degeneracy between these parameters, we generate χ^2 contour maps by sampling a uniform grid of Γ from 1.001 to 2 and f from 0 to 1 in the steps of 25. We find that for all observations these two parameters are degenerate but the degeneracy curve depends on the source position on the HID. We depict the contour plot for some of the observations from different parts of the HID in figure 4.

Due to a degeneracy in the parameter space, we cannot probe both parameters simultaneously. To understand the parameter evolution and observe the trends in different parameters as a function of time, we fix the f to a range of values 0.1, 0.3, 0.5, 0.75, and 1.0, and estimated the spectral parameters for all the observations. The evolution of the parameters is shown in figure 5. We note that not all observations result in acceptable fits (indicating a $\chi^2/\text{DoF} > 1.5$) on fixing f and the parameters of unacceptable fits are not shown in figure 5. We report the parameters for $f = 0.75$ in tables A4 and A5 as most of the observations have a $\chi^2/\text{DoF} < 1.5$.

We compute the unabsorbed flux in the energy range of 0.5–12.0 keV using the convolution model `cflux`. We use the same energy grid as we did for the `thcomp`. For computing the flux, we freeze all the parameters and then add the `cflux` component, fitting the model. Then refit the model by thawing the non-normalisation parameters (e.g. T_{in}) while keeping the Gaussian and f frozen to get

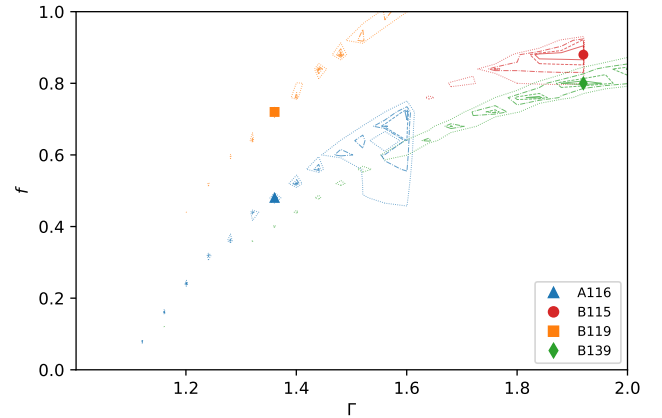


Figure 4: χ^2 contours of observations from different parts of HID, displaying the degeneracy between the parameters Γ and f are depicted in different colours. The minimum of χ^2 for each observation are indicated by different markers (and the symbol is included in the legend). We depict the contours corresponding to 68% (solid), 90% (dashed), 99% (dashed-dot) and 99.99% (dotted) confidence levels.

the flux value. The flux remains the same irrespective of f . We report the unabsorbed flux in Tables A4 and A5.

4 RESULTS AND DISCUSSION

We investigated the evolution of the continuum properties of the LMXB Aql X-1 in the soft X-rays using the *NICER* observations of the outbursts of the source in 2019 and 2020 (Outburst A and B respectively). The outbursts covered the complete evolution of the source and revealed an interesting trend in the spectral properties of the source.

4.1 Light curves and HID

The *NICER* observations of Aql X-1 in 2019 and 2020 indicate an evolution of the source which had been extensively seen in the literature (Maitra & Bailyn 2004; Güngör et al. 2014; Niwano et al. 2023). The outbursts of the source investigated here (see figure 1) are the ‘long high’ kind with the profile resembling typical fast rise exponential decay (FRED, Chen et al. 1997). Such outbursts have been seen often in Aql X-1, indicating that these outbursts are typical of the source.

Aql X-1 is known to show a Q-shaped hysteresis in its HID (using the hardness of 9.7–16/6.4–9.7 keV from *RXTE/PCA*, e.g. Maitra & Bailyn 2004) as the source evolves in the outburst. In the case of the hardness defined as 9.7–16/6.4–9.7 keV, the count rate and the hardness typically show an anti-correlation (for a higher count rate, a lower hardness was observed and vice versa). The track changes its shape when a softer definition of the hardness was used (3.8–6.8/2–3.8 keV using *NICER*, Güver et al. 2022, and 2–5/0.5–2 keV figure 2), with a change in the trend between the count rate and hardness. For the softer definition of hardness, the count rate was proportional to hardness for the majority of the observations. The trend between the hardness and intensity depends mainly on the spectral shape of the source. A positive trend indicates that with increasing count rate, the harder band has more photons than the softer band and vice versa. In case of *NICER* observations, the harder band was 2–5 keV in the current work and 3.8–6.8 keV in Güver et al. (2022) while the softer

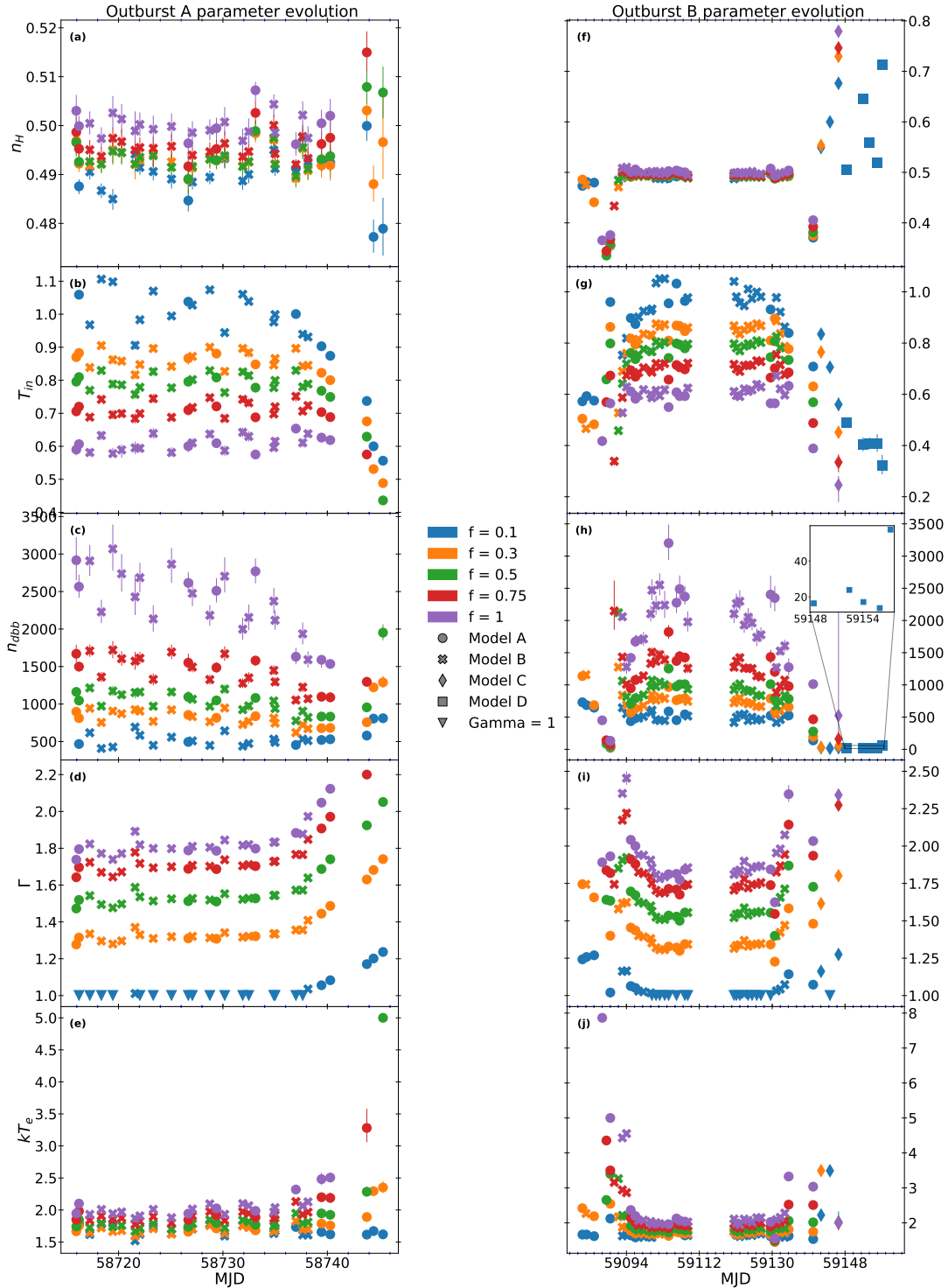


Figure 5: Spectral parameter evolution of Outburst A (Right panels) and B (left panels). Only the parameters of the observations with $\chi^2/\text{DoF} < 1.5$. Different colours are used to show the evolution of parameters for different f . The marker shapes are kept identical to figure 1. The inverted triangles in panels (d) and (i) indicate the observations which peg of $\Gamma=1$. The inset plot in panel (h) shows the disc norm evolution of the fainter observations in outburst B. The parameter values for the outbursts for $f = 0.75$ are noted in tables A4 and A5.

band was 0.5–2 keV and 2–3.8 keV respectively. Since in both of these cases, we see a positive trend between hardness and intensity, it indicated that the count rate was increasing by a larger amount in the bands 2–6.8 keV as compared to 0.5–2 keV. And the negative trend for a similar change in the count rate in 9.7–16/6.4–9.7 keV from

RXTE/PCA observations indicated in 6.4–9.7 keV band the count rates were increasing more as compared to 9.7–16 keV. Thus, in a model-independent way, we ascertain that during an outburst, there was a strong spectral change, with ≈ 2 –6 keV count rate changing

with the total count rate more strongly as compared to the energy bands around it.

The Q-shape hysteresis in Maitra & Bailyn (2004) shows that for a similar count rate, during the rise phase and the decay phase, the source could show different hardness and thus have a different spectral description. But the HID using a softer hardness ratio didn't depict the hysteresis and we observe that the path taken during the rise part of the outburst is similar to the decay part. Although the source showed jumps in hardness at similar counts (e.g. B114, B116, B150 had a higher hardness as compared to B113, B117 and B149) this is different from the traditional hysteresis where the transition from the LHS to HSS and HSS to LHS takes different paths. It was interesting to note that some of these observations have also indicated bursts (table A3).

4.2 Spectral and parameter evolution

The HID of the source indicates a clear evolution of the source throughout its outburst as it traverses through various states. In particular, the source stays for a significant amount of time in the outburst in the HSS, where the source spectrum is adequately described as a combination of a thermalised accretion disc and Compton up-scattering of a fraction of the accretion disc photons.

Due to a limited energy range covered by *NICER*, the spectral model is found to have strong degeneracies. Mainly, we found that the different combinations of photon index (Γ) and covering fraction (f) of the Comptonising medium result in similar χ^2 statistic (see figure 4 for a χ^2 contours for a sample of observations). Although there was a degeneracy between these two parameters, for individual observations the loci of the contours follow different tracks. This indicates, that although these parameters are degenerate, they have a systematic evolution as the source undergoes an outburst. Due to the degeneracy, we investigated the evolution of the parameters by fixing f for the duration of the outburst at different values.

The choice of the f did not affect the estimated value of the absorption column density (n_{H}) which has a typical value of 0.48–0.51 for almost all observations. This value is higher than the line of sight column density ($= 0.31 \times 10^{22} \text{ cm}^{-2}$, HI4PI Collaboration et al. 2016) indicating a local absorbing column. The n_{H} observed is similar to the value reported in the literature (Gusinskaia et al. 2020; Li et al. 2021). Some of the observations (B113 – B117 and B150), however, suggest that the absorption column density is similar to the line of sight value (also seen in Aql X-1 in HXMT observations in a different outburst; Güngör et al. 2020). Notably, these observations also lie on a separate part of HID (see figure 2), occupying a typically harder region for a similar count rate in rest of the observations. This behaviour suggests that the local absorption column is perhaps caused due to a clumpy medium which disappears for a small part of the outburst. And since the local absorbing column variation is independent of assumed covering fraction of the corona, we can safely assume that they are separate entities in the system.

The measurement of the temperature of the inner edge of the accretion disc (T_{in}) depends on the assumption of f . A lower covering fraction requires a hotter accretion disc for a similar fit (see figure 5). At the same time, for a lower f , the normalisation of the accretion disc component (n_{dbb}) is also lower. Barring these differences in the value offset, the trends for both parameters of the accretion disc are similar for different f . The trends for the accretion disc parameters also conform with each other in different outbursts, indicating a similar behaviour across different epochs. The evolution of T_{in} is similar to count rate and hardness evolution i.e. for the observations in HSS, the temperature remains the same. Additionally for the observations

in HSS, the disc normalization is observed to be constant indicating a stable disc during the HSS (e.g. Done et al. 2007). The *RXTE* observations have also built a similar picture of the source in the HSS (Maitra & Bailyn 2004) but the actual values differ due to the energy range considered and the model assumption used to describe the spectrum. As the source moves away from the HSS, the disc temperature reduces and the normalisation (and thus the inner radius) increases.

As expected from the χ^2 contours, Γ has a strong dependence on the assumed covering fraction. But for a given covering fraction, the Γ follows the count rate evolution inversely. For a low covering fraction, the Γ is consistent with 1.0 (see panels (d) and (i) in figure 5, where these points are indicated by triangles), which corresponds to an infinite optical depth of the corona. Electron temperature (kT_e) on the other hand is insensitive to the assumption of a fixed covering fraction (typically varying between 1.5–2 keV) but has a stronger deviation for the observations not in the HSS. In the HSS, the parameters of the corona are also roughly constant with minor fluctuations in the electron temperature which is also seen as the jitters in the source position on the HID. But as the source moves away from the HSS, the spectrum steepens with a simultaneous reduction in the accretion disc temperature and the normalization.

Some of the observations indicate residuals near 6.5 keV after modelling the spectrum with Model A. Thus we modelled these residuals with a Gaussian component to account for the Fe $K\alpha$ emission line at 6.5 keV (Reynolds & Nowak 2003). For example, for observation A116, the emission line can be clearly seen in the residuals plotted in the third panel of 3. The observations depicting significant Fe $K\alpha$ emission are marked with crosses in figures 1, 2, and 5. In all cases of detection, the line width is ≈ 0.5 keV and line normalization is $\approx 5 \times 10^{-3} \text{ photons cm}^{-2} \text{ s}^{-1}$.

5 CONCLUSIONS

We investigate the spectral properties of Aql X-1 as observed with *NICER* in 0.5–10 keV and infer the spectral components present in various canonical states of the source. The extensive *NICER* observations probed the evolution of the source using the sensitive soft X-ray coverage. The HID constructed using a softer definition of the X-ray colour revealed a track distinct from the hysteresis track typically observed for the source using a hard colour. We find that the spectrum of the source in the HSS can be well described as a partially Comptonised accretion disk. Some of the observations also exhibit reprocessing of the Comptonised emission as an iron line emission. Our analysis is limited by the degeneracy in the parameters of the Comptonising medium, likely due to limited energy range of the instrument. We find evidence for a variation in the local absorption column which also manifests as a separate position on the HID.

ACKNOWLEDGEMENTS

We express our sincere gratitude to the anonymous referee(s) for their invaluable comments and suggestions, which have significantly improved the quality and clarity of this paper. This work was supported by NASA through the *NICER* mission and the Astrophysics Explorers Program. This research has also made use of data and/or software provided by the High Energy Astrophysics Science Archive Research Center (HEASARC), which is a service of the Astrophysics Science Division at NASA/GSFC and the High Energy Astrophysics

Division of the Smithsonian Astrophysical Observatory. KGP thanks Dr Aru Beri for the help in learning HEASoft.

Table A1: *NICER* observation log for outburst A. Exposures are net exposure after the standard filtering.

DATA AVAILABILITY

The *NICER* data are available at <https://heasarc.gsfc.nasa.gov/docs/archive.html> for public download. The observation IDs mentioned in Tables A1 and A2 can be used to identify the observations in the archive.

REFERENCES

- Bhargava Y., Belloni T., Bhattacharya D., Misra R., 2019, *MNRAS*, **488**, 720
 Bhargava Y., Bhattacharyya S., Homan J., Pahari M., 2023, *arXiv e-prints*, p. [arXiv:2307.13979](https://arxiv.org/abs/2307.13979)
 Casella P., Altamirano D., Patruno A., Wijnands R., van der Klis M., 2008, *ApJ*, **674**, L41
 Chen W., Shrader C. R., Livio M., 1997, *ApJ*, **491**, 312
 Chevalier C., Ilovaisky S. A., 1991, *A&A*, **251**, L11
 Done C., Gierliński M., Kubota A., 2007, *A&ARv*, **15**, 1
 Galloway D. K., Muno M. P., Hartman J. M., Psaltis D., Chakrabarty D., 2008, *ApJS*, **179**, 360
 Gendreau K. C., et al., 2016, in *Space Telescopes and Instrumentation 2016: Ultraviolet to Gamma Ray*. p. 99051H, [doi:10.1117/12.2231304](https://doi.org/10.1117/12.2231304)
 Güngör C., Güver T., Ekşi K. Y., 2014, *MNRAS*, **439**, 2717
 Güngör C., et al., 2020, *Journal of High Energy Astrophysics*, **25**, 10
 Gusinskaia N. V., et al., 2020, *MNRAS*, **492**, 2858
 Güver T., et al., 2022, *MNRAS*, **510**, 1577
 HI4PI Collaboration et al., 2016, *A&A*, **594**, A116
 Kaastra J. S., Bleeker J. A. M., 2016, *A&A*, **587**, A151
 Kunte P. K., Durgaprasad N., Gokhale G. S., Iyengar V. S., Manchanda R. K., Sreekantan B. V., 1973, *Nature Physical Science*, **245**, 37
 Li Z., Pan Y., Falanga M., 2021, *ApJ*, **920**, 35
 López-Navas E., Degenaar N., Parikh A. S., Hernández Santisteban J. V., van den Eijnden J., 2020, *MNRAS*, **493**, 940
 Maitra D., Bailyn C. D., 2004, *ApJ*, **608**, 444
 Markwardt C., Arzoumanian Z., Gendreau K., Hare J., Rutkowski K., Loewenstein M., Nicer Team 2023, in *AAS/High Energy Astrophysics Division*. p. 103.49
 Mata Sánchez D., Muñoz-Darias T., Casares J., Jiménez-Ibarra F., 2017, *MNRAS*, **464**, L41
 Niwano M., Murata K. L., Ito N., Yatsu Y., Kawai N., 2023, *MNRAS*, **525**, 4358
 Ootes L. S., Wijnands R., Page D., Degenaar N., 2018, *MNRAS*, **477**, 2900
 Rawat D., et al., 2023, *MNRAS*, **520**, 113
 Reynolds C. S., Nowak M. A., 2003, *Phys. Rep.*, **377**, 389
 Shakura N. I., Sunyaev R. A., 1973, *A&A*, **500**, 33
 Verner D. A., Ferland G. J., Korista K. T., Yakovlev D. G., 1996, *ApJ*, **465**, 487
 Welsh W. F., Robinson E. L., Young P., 2000, *AJ*, **120**, 943
 Wilms J., Allen A., McCray R., 2000, *ApJ*, **542**, 914
 Zdziarski A. A., Szanecki M., Poutanen J., Gierliński M., Biernacki P., 2020, *MNRAS*, **492**, 5234
 Zhang L., et al., 2023, *MNRAS*, **526**, 3944
 Šimon V., 2002, *A&A*, **381**, 151
 van der Klis M., 2004, *arXiv e-prints*, [pp astro-ph/0410551](https://arxiv.org/abs/astro-ph/0410551)

APPENDIX A: TABLES

This paper has been typeset from a \LaTeX file prepared by the author.

ObsID	Start MJD	Stop MJD	Exposure(ks)
2050340102	58715.955	58715.961	0.46
2050340103	58716.214	58716.242	2.44
2050340104	58717.246	58717.269	1.99
2050340105	58718.357	58718.384	2.37
2050340106	58719.453	58719.459	0.52
2050340107	58720.297	58720.307	0.81
2050340108	58721.588	58721.593	0.4
2050340109	58722.046	58722.069	1.99
2050340110	58723.327	58723.337	0.88
2050340111	58725.076	58725.089	1.14
2050340112	58726.682	58726.686	0.41
2050340113	58727.074	58727.097	1.97
2050340114	58728.743	58728.768	2.17
2050340115	58729.376	58729.397	1.82
2050340116	58730.169	58730.178	0.77
2050340117	58731.891	58731.911	1.72
2050340118	58732.472	58732.483	0.92
2050340119	58733.117	58733.153	3.11
2050340120	58734.872	58734.910	3.28
2050340121	58734.992	58734.029	3.2
2050340122	58736.986	58736.999	1.17
2050340123	58737.64	58737.653	1.15
2050340124	58738.147	58738.165	1.54
2050340125	58739.439	58739.448	0.81
2050340126	58740.280	58740.286	0.52
2050340127	58743.777	58743.789	0.99
2050340128	58744.423	58744.434	0.96
2050340129	58745.329	58745.337	0.67

Table A2: *NICER* observation log for outburst B. Exposures are net exposure after the standard filtering.

ObsID	Start MJD	Stop MJD	Exposure(ks)
3050340108	59082.082	59082.115	2.84
3050340109	59083.115	59083.153	3.29
3050340110	59084.147	59084.201	4.64
3050340111	59084.002	59084.052	4.36
3050340112	59086.016	59086.071	4.75
3050340113	59086.002	59086.056	4.66
3050340114	59088.014	59088.074	5.14
3050340115	59089.047	59089.111	5.54
3050340116	59090.016	59090.061	3.93
3050340117	59090.984	59091.053	5.92
3050340118	59092.018	59092.073	4.79
3050340119	59093.003	59093.044	3.53
3050340120	59094.019	59094.031	1.06
3050340121	59095.069	59095.117	4.17
3050340122	59096.217	59096.256	3.39
3050340123	59097.007	59097.154	12.7
3050340124	59098.213	59098.248	2.98
3050340125	59099.991	59100.078	7.5
3050340126	59100.294	59100.332	3.26
3050340127	59101.312	59101.345	2.87
3050340128	59102.216	59102.251	3.1
3050340129	59103.444	59103.453	0.75
3050340130	59104.416	59104.424	0.75
3050340131	59106.363	59106.376	1.16
3050340132	59107.145	59107.159	1.19
3050340133	59108.432	59108.461	2.55
3050340134	59109.146	59109.157	0.99
3050340135	59120.575	59120.595	1.75
3050340136	59121.156	59121.183	2.32
3050340137	59121.992	59122.027	3.02
3050340138	59123.088	59123.113	2.15
3050340139	59124.06	59124.082	1.91
3050340140	59125.026	59125.089	5.47
3050340141	59126.188	59126.203	1.34
3050340142	59127.220	59127.245	2.17
3050340143	59129.608	59129.614	0.46
3050340144	59130.641	59130.682	3.51
3050340145	59131.032	59131.27	20.58
3050340146	59131.995	59132.135	12.11
3050340147	59133.099	59133.124	2.17
3050340148	59134.068	59134.071	0.31
3050340149	59136.379	59136.380	0.03
3050340150	59140.119	59140.131	1.05
3050340151	59142.069	59142.083	1.21
3050340152	59144.266	59144.278	1.05
3050340153	59146.379	59146.395	1.31
3050340154	59148.381	59148.394	1.17
3050340156	59152.449	59152.459	0.93
3050340157	59154.063	59154.087	2.04
3050340158	59155.937	59155.948	1.01
3050340159	59157.164	59157.173	0.81

Table A3: Log of all the burst intervals observed in the *NICER* monitoring of 2019 and 2020 outburst of the source. The time mentioned here is in spacecraft time. The mean count rate is the mean of the count rate before the outburst. The peak count rate is the peak count rate of the burst. For the observation 3050340116, the decay of a burst is observed, so the peak count rate is uncertain.

ObsID	Time interval (in s)	Duration(s)	Mean count rate	Peak count rate
3050340110	209658056-209658596	540	585.85	5497.43
3050340111	209719346-209719646	300	398.96	3237.50
3050340114	209998142-209998642	500	161.68	3627.87
3050340116	210154101-210154293	192	130.91	186.37
3050340123	210767412-210767912	500	1857.85	2225.94
3050340142	213346189-213346299	110	2700.36	4324.25
3050340150	214455474-214455554	80	268.22	1566.81
3050340150	214455934-214455974	40	246.02	1664.31

Table A4: Outburst A (2019) spectral parameter table for $f=0.75$ assuming the models: Model A: $\text{tbabs}^*(\text{gauss}+\text{thcomp}\otimes\text{diskbb})$ and Model B: $\text{tbabs}^*(\text{gauss}+\text{gauss}+\text{thcomp}\otimes\text{diskbb})$. Errors listed here are 1σ errors and they are not listed for the observations with $\chi^2/\text{DoF} > 1.5$ and for parameter with error of the order 0.001.

ID	n_H^δ	Gaussian (6.5 keV) ^{α}		diskbb		thcomp		Flux ^{β}	
		Sigma (keV)	norm (10^{-3})	T_{in} (keV)	n_{dbb} (10^2)	Γ	kT_e (keV)	$10^{-8}\text{erg/cm}^2/\text{s}$	χ^2 / DoF
A102	0.5	–	–	0.71 ^{+0.01} _{–0.01}	16.69 ^{+1.2} _{–1.1}	1.64 ^{+0.01} _{–0.01}	1.85 ^{+0.02} _{–0.02}	1.869 ^{+0.004} _{–0.004}	146 / 142
A103	0.5	–	–	0.72 ^{+0.01} _{–0.01}	14.98 ^{+0.7} _{–0.6}	1.7 ^{+0.01} _{–0.01}	1.98 ^{+0.02} _{–0.02}	1.74 ^{+0.002} _{–0.002}	119 / 153
A104	0.5	0.44 ^{+0.08} _{–0.07}	5.1 ^{+0.8} _{–1.0}	0.69 ^{+0.01} _{–0.01}	17.09 ^{+0.8} _{–0.8}	1.72 ^{+0.01} _{–0.01}	1.84 ^{+0.02} _{–0.02}	1.609 ^{+0.002} _{–0.002}	147 / 152
A105	0.49	0.43 ^{+0.1} _{–0.08}	4.1 ^{+0.5} _{–0.9}	0.74 ^{+0.01} _{–0.01}	13.6 ^{+0.6} _{–0.7}	1.67 ^{+0.01} _{–0.01}	1.91 ^{+0.02} _{–0.02}	1.792 ^{+0.002} _{–0.002}	135 / 154
A106	0.5	0.5 [*]	6.5 ^{+1.6} _{–1.6}	0.7 ^{+0.01} _{–0.01}	17.2 ^{+1.2} _{–1.1}	1.64 ^{+0.01} _{–0.01}	1.85 ^{+0.03} _{–0.02}	1.822 ^{+0.004} _{–0.004}	131 / 145
A107	0.5	0.52 ^{+0.25} _{–0.14}	4.9 ^{+2.5} _{–1.6}	0.7 ^{+0.01} _{–0.01}	16.04 ^{+1.0} _{–0.9}	1.67 ^{+0.01} _{–0.01}	1.87 ^{+0.02} _{–0.02}	1.69 ^{+0.003} _{–0.003}	154 / 147
A108	0.49	0.65 ^{+0.19} _{–0.15}	7.8 ^{+3.1} _{–2.3}	0.68 ^{+0.02} _{–0.01}	15.72 ^{+1.2} _{–1.1}	1.78 ^{+0.02} _{–0.01}	1.78 ^{+0.04} _{–0.03}	1.366 ^{+0.003} _{–0.003}	137 / 137
A109	0.5	0.62 ^{+0.11} _{–0.1}	7.1 ^{+1.6} _{–1.4}	0.7 ^{+0.01} _{–0.01}	16.11 ^{+0.8} _{–0.8}	1.72 ^{+0.01} _{–0.01}	1.82 ^{+0.02} _{–0.02}	1.611 ^{+0.002} _{–0.002}	139 / 152
A110	0.5	0.7 ^{+0.21} _{–0.17}	6.0 ^{+2.7} _{–2.0}	0.74 ^{+0.01} _{–0.01}	13.28 ^{+0.8} _{–0.8}	1.69 ^{+0.01} _{–0.01}	1.9 ^{+0.03} _{–0.02}	1.728 ^{+0.003} _{–0.003}	112 / 148
A111	0.5	0.45 ^{+0.11} _{–0.1}	4.6 ^{+1.3} _{–1.2}	0.69 ^{+0.01} _{–0.01}	16.93 ^{+1.0} _{–0.9}	1.7 ^{+0.01} _{–0.01}	1.8 ^{+0.02} _{–0.02}	1.614 ^{+0.003} _{–0.003}	162 / 150
A112	0.49	–	–	0.71 ^{+0.02} _{–0.02}	15.51 ^{+1.2} _{–1.1}	1.69 ^{+0.01} _{–0.01}	1.85 ^{+0.03} _{–0.03}	1.69 ^{+0.004} _{–0.004}	150 / 141
A113	0.49	0.42 ^{+0.07} _{–0.06}	5.2 ^{+1.0} _{–0.9}	0.72 ^{+0.01} _{–0.01}	14.93 ^{+0.7} _{–0.7}	1.71 ^{+0.01} _{–0.01}	1.91 ^{+0.02} _{–0.02}	1.679 ^{+0.002} _{–0.002}	138 / 152
A114	0.49	0.64 ^{+0.15} _{–0.13}	6.8 ^{+2.0} _{–1.6}	0.75 ^{+0.01} _{–0.01}	13.25 ^{+0.6} _{–0.6}	1.7 ^{+0.01} _{–0.01}	1.98 ^{+0.02} _{–0.02}	1.754 ^{+0.002} _{–0.002}	121 / 153
A115	0.5	–	–	0.72 ^{+0.01} _{–0.01}	14.86 ^{+0.7} _{–0.6}	1.69 ^{+0.01} _{–0.01}	1.92 ^{+0.02} _{–0.02}	1.735 ^{+0.002} _{–0.002}	184 / 154
A116	0.5	0.61 ^{+0.14} _{–0.12}	8.9 ^{+2.5} _{–2.0}	0.68 ^{+0.01} _{–0.01}	16.7 ^{+1.0} _{–1.0}	1.74 ^{+0.01} _{–0.01}	1.84 ^{+0.03} _{–0.02}	1.52 ^{+0.003} _{–0.003}	133 / 145
A117	0.49	0.54 ^{+0.13} _{–0.11}	4.7 ^{+1.4} _{–1.2}	0.74 ^{+0.01} _{–0.01}	12.77 ^{+0.6} _{–0.6}	1.7 ^{+0.01} _{–0.01}	1.97 ^{+0.02} _{–0.02}	1.642 ^{+0.002} _{–0.002}	97 / 152
A118	0.49	0.42 ^{+0.18} _{–0.14}	3.9 ^{+1.8} _{–1.3}	0.73 ^{+0.01} _{–0.01}	13.49 ^{+0.8} _{–0.8}	1.71 ^{+0.01} _{–0.01}	1.95 ^{+0.03} _{–0.03}	1.633 ^{+0.003} _{–0.003}	183 / 150
A119	0.5	–	–	0.69 ^{+0.01} _{–0.01}	15.79 ^{+0.5} _{–0.7}	1.7 ^{+0.01} _{–0.01}	1.89 ^{+0.01} _{–0.01}	1.522 ^{+0.003} _{–0.003}	180 / 154
A120	0.5	0.51 ^{+0.08} _{–0.07}	5.5 ^{+1.0} _{–0.9}	0.7 ^{+0.01} _{–0.01}	14.48 ^{+0.7} _{–0.6}	1.73 ^{+0.01} _{–0.01}	1.87 ^{+0.02} _{–0.02}	1.436 ^{+0.003} _{–0.003}	107 / 153
A121	0.49	0.62 ^{+0.15} _{–0.13}	4.3 ^{+1.3} _{–1.1}	0.72 ^{+0.01} _{–0.01}	12.95 ^{+0.6} _{–0.6}	1.73 ^{+0.01} _{–0.01}	1.92 ^{+0.02} _{–0.02}	1.445 ^{+0.002} _{–0.002}	114 / 154
A122	0.49	0.02 ^{+0.08} _{–0.02}	0.6 ^{+0.3} _{–0.3}	0.75 ^{+0.01} _{–0.02}	10.52 ^{+0.5} _{–0.5}	1.77 ^{+0.01} _{–0.01}	2.13 ^{+0.03} _{–0.03}	1.365 ^{+0.002} _{–0.002}	114 / 149
A123	0.5	0.69 ^{+0.25} _{–0.18}	4.4 ^{+2.2} _{–1.6}	0.71 ^{+0.01} _{–0.01}	12.25 ^{+0.6} _{–0.6}	1.77 ^{+0.01} _{–0.01}	1.93 ^{+0.03} _{–0.03}	1.237 ^{+0.002} _{–0.002}	132 / 148
A124	0.49	0.7 ^{+0.13} _{–0.11}	6.0 ^{+1.6} _{–1.3}	0.72 ^{+0.01} _{–0.01}	10.7 ^{+0.6} _{–0.5}	1.85 ^{+0.01} _{–0.01}	1.97 ^{+0.03} _{–0.03}	1.109 ^{+0.002} _{–0.002}	116 / 148
A125	0.5	–	–	0.7 ^{+0.01} _{–0.01}	10.97 ^{+0.6} _{–0.5}	1.91 ^{+0.01} _{–0.01}	2.2 ^{+0.06} _{–0.05}	1.001 ^{+0.002} _{–0.002}	158 / 141
A126	0.5	–	–	0.69 ^{+0.01} _{–0.01}	10.89 ^{+0.7} _{–0.7}	1.97 ^{+0.02} _{–0.02}	2.19 ^{+0.08} _{–0.07}	0.875 ^{+0.003} _{–0.003}	130 / 136
A127	0.51	–	–	0.58 ^{+0.01} _{–0.01}	12.95 ^{+0.7} _{–0.6}	2.2 ^{+0.02} _{–0.02}	3.28 ^{+0.3} _{–0.22}	0.469 ^{+0.001} _{–0.001}	183 / 137
A128 [†]	0.5	–	–	0.49	16.7	1.98	131.1	0.303	487 / 135
A129 [†]	0.52	–	–	0.35	42.37	2.24	3.5	0.22	373 / 126

* frozen to the values.

† observations with $\chi^2/\text{DoF} > 1.5$.

δ The 1σ errors for n_H are ≈ 0.002 .

α The Gaussian line energy for Fe $K\alpha$ line is fixed at 6.5 keV.

β The flux is the unabsorbed flux computed in the energy range 0.5–12 keV.

γ The instrumental Gaussian is present in all the observations at around 0.75 keV with a width of ≈ 0.04 keV.

Table A5: Outburst B (2020) spectral parameter table for $f=0.75$. assuming the models: Model A: $\text{tbabs}^*(\text{gauss}+\text{thcomp}\otimes\text{diskbb})$, Model B: $\text{tbabs}^*(\text{gauss}+\text{gauss}+\text{thcomp}\otimes\text{diskbb})$, Model C: $\text{tbabs}^*(\text{thcomp}\otimes\text{diskbb})$, Model D: $\text{tbabs}^*(\text{diskbb})$. Rest of the configuration is same as table A4.

ID	n_H^δ	Gaussian (6.5 keV) $^\alpha$		diskbb		thcomp		Flux $^\beta$	
		Sigma (keV)	norm (10^{-3})	T_{in} (keV)	$n_{\text{dbb}}(10^2)$	Γ	kT_e (keV)	(10^{-8} erg/cm 2 /s)	χ^2 / DoF
B108 †	0.48	–	–	0.38	20.39	2.03	79.25	0.135	786 / 137
B109 †	0.5	–	–	0.46	15.81	2.04	150.0	0.217	268 / 140
B110 †	0.5	–	–	0.49	13.34	2.1	119.97	0.229	467 / 142
B111 †	0.49	1.1	2.4	0.42	17.94	2.14	71.42	0.161	769 / 140
B112 †	0.5	–	–	0.48	12.63	2.14	108.74	0.189	453 / 140
B113 †	0.46	–	–	0.42	11.25	1.95	114.46	0.119	219 / 138
B114 †	0.36	–	–	0.53	2.04	1.81	3.55	0.072	233 / 137
B115	0.34	–	–	0.57 $^{+0.01}_{-0.01}$	1.4 $^{+0.1}_{-0.1}$	1.84 $^{+0.01}_{-0.01}$	4.36 $^{+0.78}_{-0.45}$	0.064	175 / 135
B116	0.37	–	–	0.67 $^{+0.01}_{-0.01}$	0.74	1.82 $^{+0.01}_{-0.01}$	3.5*	0.066	163 / 134
B117	0.43 $^{+0.01}_{-0.01}$	0.5*	0.3 $^{+0.1}_{-0.1}$	0.34 $^{+0.01}_{-0.02}$	21.47 $^{+4.7}_{-2.9}$	1.74 $^{+0.01}_{-0.01}$	3.16 $^{+0.09}_{-0.08}$	0.155	153 / 144
B118 †	0.49	0.5*	2.0	0.44	25.36	1.94	53.37	0.332	281 / 148
B119	0.5	0.5*	2.5 $^{+0.3}_{-0.3}$	0.59 $^{+0.01}_{-0.01}$	14.32 $^{+0.4}_{-0.5}$	2.17 $^{+0.01}_{-0.01}$	2.94 $^{+0.12}_{-0.1}$	0.567 $^{+0.001}_{-0.001}$	181 / 150
B120	0.5	0.5*	3.7 $^{+0.5}_{-0.5}$	0.67 $^{+0.01}_{-0.01}$	10.1 $^{+0.5}_{-0.4}$	2.22 $^{+0.02}_{-0.02}$	2.86 $^{+0.21}_{-0.17}$	0.665 $^{+0.002}_{-0.002}$	106 / 139
B121	0.5	–	–	0.69 $^{+0.01}_{-0.01}$	9.47 $^{+0.4}_{-0.3}$	1.91 $^{+0.01}_{-0.01}$	2.14 $^{+0.03}_{-0.03}$	0.813 $^{+0.001}_{-0.001}$	145 / 153
B122	0.5	–	–	0.67 $^{+0.01}_{-0.01}$	10.75 $^{+0.4}_{-0.4}$	1.88 $^{+0.01}_{-0.01}$	2.02 $^{+0.02}_{-0.03}$	0.815 $^{+0.001}_{-0.001}$	149 / 153
B123	0.5	0.56 $^{+0.08}_{-0.07}$	3.3 $^{+0.5}_{-0.5}$	0.68 $^{+0.01}_{-0.01}$	10.91 $^{+0.4}_{-0.4}$	1.83 $^{+0.01}_{-0.01}$	1.93 $^{+0.01}_{-0.01}$	0.933	117 / 167
B124	0.5	0.33 $^{+0.1}_{-0.08}$	2.2 $^{+0.6}_{-0.5}$	0.7 $^{+0.01}_{-0.01}$	11.4 $^{+0.5}_{-0.5}$	1.82 $^{+0.01}_{-0.01}$	1.94 $^{+0.02}_{-0.02}$	1.091 $^{+0.001}_{-0.001}$	93 / 152
B125	0.5	0.47 $^{+0.07}_{-0.07}$	3.8 $^{+0.6}_{-0.6}$	0.69 $^{+0.01}_{-0.01}$	13.32 $^{+0.5}_{-0.5}$	1.79 $^{+0.01}_{-0.01}$	1.92 $^{+0.01}_{-0.01}$	1.229	109 / 161
B126	0.5	0.54 $^{+0.14}_{-0.11}$	2.6 $^{+0.9}_{-0.7}$	0.69 $^{+0.01}_{-0.01}$	15.06 $^{+0.7}_{-0.6}$	1.75 $^{+0.01}_{-0.01}$	1.86 $^{+0.01}_{-0.02}$	1.373	101 / 152
B127	0.49	0.35 $^{+0.08}_{-0.07}$	3.1 $^{+0.7}_{-0.7}$	0.72 $^{+0.01}_{-0.01}$	13.65 $^{+0.6}_{-0.6}$	1.7 $^{+0.01}_{-0.01}$	1.9 $^{+0.02}_{-0.02}$	1.562 $^{+0.002}_{-0.002}$	114 / 153
B128	0.5	0.62 $^{+0.2}_{-0.15}$	4.7 $^{+1.9}_{-1.3}$	0.71 $^{+0.01}_{-0.01}$	14.7 $^{+0.7}_{-0.7}$	1.69 $^{+0.01}_{-0.01}$	1.88 $^{+0.01}_{-0.01}$	1.604	114 / 153
B129	0.49	0.56 $^{+0.28}_{-0.18}$	4.2 $^{+2.5}_{-1.7}$	0.72 $^{+0.01}_{-0.01}$	13.91 $^{+0.9}_{-0.9}$	1.69 $^{+0.01}_{-0.01}$	1.87 $^{+0.03}_{-0.02}$	1.603 $^{+0.003}_{-0.002}$	135 / 145
B130	0.5	–	–	0.66 $^{+0.01}_{-0.01}$	18.21 $^{+1.1}_{-1.1}$	1.71 $^{+0.01}_{-0.01}$	1.85 $^{+0.02}_{-0.01}$	1.464 $^{+0.003}_{-0.003}$	148 / 145
B131	0.5	–	–	0.71 $^{+0.01}_{-0.01}$	13.71 $^{+0.7}_{-0.7}$	1.71 $^{+0.01}_{-0.01}$	1.99 $^{+0.02}_{-0.02}$	1.529 $^{+0.003}_{-0.003}$	126 / 150
B132	0.5	–	–	0.71 $^{+0.01}_{-0.01}$	14.45 $^{+0.8}_{-0.7}$	1.68 $^{+0.01}_{-0.01}$	1.95 $^{+0.02}_{-0.02}$	1.582 $^{+0.003}_{-0.003}$	132 / 151
B133	0.5	–	–	0.7 $^{+0.01}_{-0.01}$	14.23 $^{+0.6}_{-0.6}$	1.74 $^{+0.01}_{-0.01}$	1.92 $^{+0.02}_{-0.02}$	1.402 $^{+0.002}_{-0.002}$	129 / 153
B134	0.49	0.63 $^{+0.13}_{-0.11}$	7.5 $^{+2.0}_{-1.7}$	0.72 $^{+0.01}_{-0.01}$	12.56 $^{+0.7}_{-0.7}$	1.74 $^{+0.01}_{-0.01}$	1.9 $^{+0.03}_{-0.03}$	1.395 $^{+0.003}_{-0.003}$	109 / 147
B135	0.49	0.61 $^{+0.22}_{-0.25}$	4.1 $^{+1.9}_{-1.6}$	0.72 $^{+0.01}_{-0.01}$	12.74 $^{+0.7}_{-0.6}$	1.71 $^{+0.01}_{-0.01}$	1.98 $^{+0.02}_{-0.02}$	1.446 $^{+0.002}_{-0.002}$	118 / 151
B136	0.49	0.21 $^{+0.07}_{-0.05}$	2.2 $^{+0.6}_{-0.5}$	0.7 $^{+0.01}_{-0.01}$	13.7 $^{+0.6}_{-0.6}$	1.73 $^{+0.01}_{-0.01}$	1.89 $^{+0.02}_{-0.02}$	1.374 $^{+0.001}_{-0.001}$	114 / 152
B137	0.5	0.56 $^{+0.1}_{-0.09}$	4.5 $^{+1.0}_{-0.9}$	0.69 $^{+0.01}_{-0.01}$	14.22 $^{+0.7}_{-0.6}$	1.73 $^{+0.01}_{-0.01}$	1.85 $^{+0.02}_{-0.02}$	1.336 $^{+0.002}_{-0.002}$	122 / 153
B138	0.49	0.49 $^{+0.12}_{-0.1}$	3.6 $^{+1.0}_{-0.9}$	0.71 $^{+0.01}_{-0.01}$	12.59 $^{+0.6}_{-0.6}$	1.78 $^{+0.01}_{-0.01}$	1.97 $^{+0.02}_{-0.02}$	1.299 $^{+0.002}_{-0.002}$	110 / 152
B139	0.5	0.23 $^{+0.08}_{-0.05}$	1.8 $^{+0.6}_{-0.5}$	0.71 $^{+0.01}_{-0.01}$	12.59 $^{+0.6}_{-0.6}$	1.72 $^{+0.01}_{-0.01}$	1.95 $^{+0.02}_{-0.02}$	1.384 $^{+0.002}_{-0.002}$	141 / 152
B140	0.5	0.58 $^{+0.11}_{-0.05}$	4.2 $^{+1.0}_{-0.9}$	0.71 $^{+0.01}_{-0.01}$	12.52 $^{+0.6}_{-0.5}$	1.74 $^{+0.01}_{-0.01}$	1.91 $^{+0.02}_{-0.01}$	1.332	102 / 156
B141	0.49	0.48 $^{+0.15}_{-0.1}$	4.6 $^{+1.5}_{-1.1}$	0.73 $^{+0.01}_{-0.01}$	11.41 $^{+0.6}_{-0.6}$	1.74 $^{+0.01}_{-0.01}$	2.0 $^{+0.03}_{-0.03}$	1.344 $^{+0.002}_{-0.002}$	124 / 149
B142	0.49	0.65 $^{+0.27}_{-0.21}$	4.5 $^{+2.3}_{-1.6}$	0.73 $^{+0.01}_{-0.01}$	11.23 $^{+0.6}_{-0.6}$	1.76 $^{+0.01}_{-0.01}$	2.0 $^{+0.02}_{-0.02}$	1.286 $^{+0.002}_{-0.002}$	138 / 152
B143	0.5	–	–	0.67 $^{+0.01}_{-0.01}$	14.32 $^{+1.1}_{-1.0}$	1.74 $^{+0.01}_{-0.01}$	1.9 $^{+0.03}_{-0.03}$	1.183 $^{+0.003}_{-0.003}$	132 / 138
B144	0.49	–	–	0.7 $^{+0.01}_{-0.01}$	12.03 $^{+0.7}_{-0.8}$	1.55 $^{+0.01}_{-0.01}$	1.51 $^{+0.01}_{-0.01}$	1.363 $^{+0.001}_{-0.001}$	191 / 155
B145	0.49	0.56 $^{+0.07}_{-0.06}$	3.3 $^{+0.5}_{-0.5}$	0.76 $^{+0.01}_{-0.01}$	8.81 $^{+0.3}_{-0.3}$	1.83 $^{+0.01}_{-0.01}$	1.96 $^{+0.01}_{-0.01}$	1.089	125 / 172
B146	0.49	0.69 $^{+0.07}_{-0.07}$	4.7 $^{+0.7}_{-0.6}$	0.71 $^{+0.01}_{-0.01}$	9.76 $^{+0.2}_{-0.3}$	1.87 $^{+0.01}_{-0.01}$	2.01 $^{+0.02}_{-0.02}$	0.959	122 / 167
B147	0.49	0.75 $^{+0.17}_{-0.16}$	4.7 $^{+1.5}_{-1.2}$	0.68 $^{+0.01}_{-0.01}$	10.74 $^{+0.2}_{-0.5}$	1.94 $^{+0.01}_{-0.01}$	2.06 $^{+0.04}_{-0.04}$	0.814 $^{+0.001}_{-0.001}$	108 / 149
B148	0.5	–	–	0.69 $^{+0.01}_{-0.01}$	9.78 $^{+0.8}_{-0.7}$	2.14 $^{+0.03}_{-0.03}$	2.52 $^{+0.22}_{-0.18}$	0.708	149 / 130
B150	0.39 $^{+0.01}_{-0.01}$	–	–	0.49 $^{+0.02}_{-0.02}$	4.66 $^{+0.6}_{-0.5}$	1.94 $^{+0.02}_{-0.02}$	2.51 $^{+0.21}_{-0.16}$	0.105	121 / 119
B151 †	0.58	–	–	0.58	0.77	2.06	2.5	0.031	180 / 117
B152 †	0.66	–	–	0.38	1.26	2.09	2.0	0.013	319 / 107
B153	0.75 $^{+0.04}_{-0.04}$	–	–	0.33 $^{+0.03}_{-0.02}$	1.61 $^{+1.3}_{-0.5}$	2.27 $^{+0.04}_{-0.03}$	2.0	0.006	123 / 96
B154	0.5 $^{+0.03}_{-0.03}$	–	–	0.49 $^{+0.02}_{-0.02}$	0.16 $^{+0.003}_{-0.003}$	–	–	0.001	38 / 41
B156	0.64 $^{+0.06}_{-0.05}$	–	–	0.4 $^{+0.03}_{-0.03}$	0.23 $^{+0.1}_{-0.1}$	–	–	0.001	22 / 25
B157	0.56 $^{+0.05}_{-0.04}$	–	–	0.41 $^{+0.02}_{-0.02}$	0.17 $^{+0.1}_{-0.1}$	–	–	0.001	17 / 22
B158	0.52 $^{+0.08}_{-0.07}$	–	–	0.41 $^{+0.04}_{-0.03}$	0.13 $^{+0.1}_{-0.1}$	–	–	0.001	31 / 24
B159	0.71 $^{+0.13}_{-0.11}$	–	–	0.32 $^{+0.04}_{-0.04}$	0.57 $^{+0.8}_{-0.3}$	–	–	0.001	14 / 16

* frozen to the values.

† observations with $\chi^2/\text{DoF} > 1.5$.

$^\delta$ The 1σ errors for n_H are ≈ 0.002 .

$^\alpha$ The Gaussian line energy for Fe $k\alpha$ line is fixed at 6.5 keV.

$^\beta$ The flux is the unabsorbed flux computed in the energy range 0.5–12 keV.

$^\gamma$ The instrumental Gaussian is present in all the observations (except B151–B159) at around 0.75 keV with a width of ≈ 0.04 keV.